

Identifying signatures of photothermal current in a double-gated semiconducting nanotube

G. Buchs^{1,*}, S. Bagiante², G. A. Steele^{3,*}

¹Centre Suisse d'Electronique et de Microtechnique (CSEM), Jaquet-Droz 1, 2002 Neuchâtel, Switzerland.

²Laboratory for Micro- and Nanotechnology, Paul Scherrer Institut, 5232 Villigen PSI, Switzerland.

³Kavli Institute of NanoScience, Delft University of Technology, PO Box 5046, 2600 GA, Delft, The Netherlands.

*Correspondence and requests for materials should be address to G.A.S. and/or G.B.

(email: g.a.steele@tudelft.nl; gilles.buchs@csem.ch).

The remarkable electrical and optical properties of single-walled carbon nanotubes (SWNT) have allowed for engineering device prototypes showing great potential for applications such as photodectors and solar cells. However, any path towards industrial maturity requires a detailed understanding of the fundamental mechanisms governing the process of photocurrent generation. Here, we present scanning photocurrent microscopy measurements on a double-gated suspended semiconducting SWNT and show that both photovoltaic and photothermal mechanisms are relevant for the interpretation of the photocurrent. We find that the dominant or non-dominant character of one or the other processes depends on the doping profile, and that the magnitude of each contribution is strongly influenced by the series resistance from the band alignment with the metal contacts. These results provide new insight into the interpretation of features in scanning photocurrent microscopy and lay the foundation for the understanding of optoelectronic devices made from SWNTs.

Introduction

A better understanding of charge transport mechanisms in nanoscale devices, especially the role of electrical contact interfaces and band bending, has been made possible in the last decade with the development of scanning photocurrent microscopy (SPCM), a dedicated local probe technique exploiting local electrical currents generation from light absorption. This technique has been used for characterizing various systems like *e.g.* Si nanowires [1, 2, 3], colloidal quantum dots [4], VO₂ nanobeams [5], carbon nanotubes [6, 7, 8, 9, 10, 11, 12, 13, 15] as well as 2D materials like graphene [16, 17, 18, 19, 20, 21, 22, 23] and MoS₂ [24, 25]. In such nanoscale systems, two mechanisms have been identified for the generation of photocurrent: i) photovoltaic processes where photo-excited carriers are separated by built-in electrical fields and ii) photothermal processes where thermoelectric forces drive carriers through light-induced thermal gradients.

Single-walled carbon nanotubes (SWNT) are long, one dimensional conductors with a band structure ranging from quasimetallic (bandgap $E_g \sim 30$ meV) to semiconducting character (E_g typically in the range of 0.1 to 1 eV) depending on chirality and diameter. These properties make SWNTs an ideal platform for exploring photocurrent generation with SPCM. In early single-walled nanotubes SPCM work the interpretation of photocurrent was mostly based on photovoltaic mechanisms [6, 7, 8, 9, 11]. The importance of photothermal effects has been suggested in the context of measurements of bulk SWNT films [12, 13, 14] and very recently, SPCM work on graphene and individual metallic SWNTs has emphasized the importance of photothermal mechanisms in materials with no or small bandgaps [22, 26]. The question of the role of photothermal mechanisms in larger bandgap semiconducting nanotubes has been studied very recently in double-gated [26] and single-gated [27] suspended carbon nanotube devices. These two studies report contradictory results, leaving the understanding of fundamental mechanisms underlying photocurrent generation in semiconducting nanotubes unclear.

Here we report on the study of a suspended semiconducting nanotube device where we show that both photovoltaic and photothermal mechanisms compete in the generation of photocurrent. In particular, we find that the dominant or non-dominant character of one or the other processes is a function of the doping profile and that the magnitude of each contribution is strongly influenced by the band alignment with the metal contacts through the resulting contact resistance.

Results

Description of the device. The device consists of a suspended nanotube grown between platinum electrodes over a predefined $3\ \mu\text{m}$ wide and $1\ \mu\text{m}$ deep trench with four gates defined at the bottom (see Methods). A schematic and a scanning electron microscopy image of a typical device used in this study are shown in Figs. 1(a) and 1(b), respectively. In our SPCM experiments, gate pairs G1-G2 and G3-G4 are connected to independent tunable voltage sources $V_{\text{G1-G2}}$ and $V_{\text{G3-G4}}$, respectively and source-drain voltage V_{SD} is set to 0 V. All measurements are performed at atmospheric pressure and room temperature. A transistor characteristic curve of the device recorded by sweeping all gate voltages simultaneously with $V_{\text{SD}} = 1\ \text{mV}$ is displayed in Fig. 1(c). A large conductance for holes ($R \approx 300\text{k}\Omega$) and a very low conductance for electrons ($R > \text{G}\Omega$) are observed. From the largely suppressed conductance when the device is pinched-off, we conclude that the nanotube is semiconducting with a relatively large bandgap of the order of a few to several hundreds of meV [15], consistent with the diameter distribution expected from the growth recipe used [28].

SPCM Measurements. Photocurrent (PC) images and corresponding qualitative band diagrams for p-n, n-n, and p-p doping configurations are shown in Fig. 2. For n-n and p-n (n-p) configurations, strong PC signatures observed at locations corresponding to local depletion regions show signs which are consistent with photovoltaic processes [15, 7]. The PC image for the p-p configuration shows a more complex pattern with alternating sign changes along the nanotube axis. The sign of PC spots at the drain and source electrode edges is consistent with the photovoltaic mechanism. However, the sign of the PC patterns observed inside the trench cannot be explained even qualitatively by photovoltaic effects, since it indicates that electrons are travelling “uphill” along the electrostatic potential profile. Similar observations have recently been reported for single gated devices and have been attributed to photothermoelectric effects [27].

In order to explore the possibility of the presence of such photothermoelectric effects in our device, we studied the PC generation mechanisms by inducing non-uniform charge density profiles in the suspended nanotube channel using the two separate gate pairs. For this, we recorded 2D maps of the PC as a function of the gate pairs voltages ($V_{\text{G1-G2}}$ and $V_{\text{G2-G3}}$) for a fixed location of the laser spot along the nanotube axis. The resulting 2D map for the laser spot located at the center of the suspended portion of the SWNT is shown in Fig. 3(a). Four doping regions, clockwise p-n, n-n, n-p and p-p, are identified

across the gates voltages space and are delimited by two dashed black lines. A first clear feature of the image is a strongly suppressed PC in the n-n region. This can be easily understood from the very high contact resistance ($R > G\Omega$) measured in this regime (Fig. 1(c)). The p-n and n-p regions show PC signatures with a sign that is consistent with the photovoltaic mechanism (Note that the slight clockwise tilt angle of the strip shaped pattern is most probably due to the fact that the laser spot is not exactly centred on the n-p (or p-n) depletion zone but slightly shifted towards the drain contact. This has no incidence on the main conclusions of our present work). However, the p-p region shows PC features which are not consistent with a purely photovoltaic mechanism. This can be verified if one considers the line trace in Fig. 3(b) corresponding to a transition from p-n to p-p⁺ doping configuration along the vertical dashed line in the PC map, which reveals two sign reversals of the PC signal. From a purely photovoltaic mechanism, one would expect a monotonic increase of the PC signal from the p-n minimum to a positive value in the p-p⁺ region with a zero crossing at the symmetric p-p doping profile. This would show only one single PC sign reversal corresponding to a sign reversal of the electric field at the laser spot location. The exact same analysis applies for the PC signal recorded along the horizontal dashed line in the 2D map (Fig. 3(c)).

Model for photothermal currents. From the above analysis, it is clear that the photocurrent in the p-p region of Fig. 3 cannot be described by a photovoltaic mechanism, even at a qualitative level. In Fig. 4, we show how the observations in Fig. 3 can be explained with a simple model where the suspended nanotube is separated in two regions of different carriers density on the left and right side of the laser spot. The model also includes the effect of laser heating at the junction between the two regions. The left (drain contact) and right (source contact) portions have average Seebeck coefficients S_1 and S_2 , respectively. The laser light induces a temperature increase ΔT with respect to the contacts which can be regarded as heat sinks. We consider linear temperature profiles from the $S_1 - S_2$ interface to the contacts [27, 12]. Photothermal currents are induced by the local electromotive field $\mathbf{E}_{PT} = -S\nabla T$ where ∇T is the temperature gradient along the nanotube axis and S is the Seebeck coefficient. Thus the generated photothermal current can be expressed by $I_{PT} = -R^{-1} \cdot \int S(x)\nabla T dx$ where R is the overall contact resistance. Applied to our thermocouple model, we find:

$$I_{PT} = R^{-1} \cdot |\Delta T| \cdot (S_2 - S_1) \quad (1)$$

The sign of the above expression (conventional flow notation) is then given by the Seebeck coefficients

, whose absolute values and signs depend on the doping levels. A qualitative profile of the Seebeck coefficient as a function of the Fermi level for a semiconducting SWNT is shown in Fig. 4(a) [29, 27].

Analysis and interpretation of the experimental results. Band diagrams corresponding to doping configurations along the vertical line in Fig. 3(a), *i.e.* p-n, p-p⁻ and p-p⁺ are drawn in Figs. 4(c)-(e), respectively. The photothermal and photovoltaic currents are indicated with arrows oriented with respect to the electronic flow notation (colors correspond to the current sign with respect to the conventional flow notation, *i.e.* red for positive and blue for negative). From this, we find that the photovoltaic and photothermal currents in the case of the p-n (and n-p) configuration flow in the same direction. However, we find that photovoltaic and photothermal currents are flowing in opposite directions for p-p⁻ and p-p⁺ (p⁻-p and p⁺-p). To understand these opposite flowing currents, it is important to contrast the mechanisms driving the two. For photovoltaic currents, electron flow is driven by differences in electrostatic voltage: electrons move to the point of lowest energy. For photothermal currents, electrons are driven by differences in chemical potential and in some cases can cause electrons to flow “uphill“. The photothermal current signs given by our model for gates voltages configurations corresponding to a p-doped nanotube channel (Fig. 4(d)-(e)) are consistent with the experimental results (p-p region in Fig. 3(a)), indicating that photothermoelectric effects are dominant in our device in this regime. From equation 1 and the maximum PC in the p-p region of about 20 pA corresponding to a Seebeck coefficient difference $S_2 - S_1 \approx 140 \mu\text{V}/\text{K}$ [29], we estimate the laser-induced temperature increase ΔT to be in the order of ~ 50 mK. This is smaller than what was reported in a previous work [26]. This could be a result of the approximation of an abrupt junction in our model, from different net laser power reaching the sample, or from a different ratio between excitation energy and optical resonances of the nanotube.

From the data in Fig. 3, it is also quite clear that the largest photocurrent occurs in the p-p region, suggesting that photothermal mechanisms are the most dominant in our device for all gate voltages. However, we note that one has to be careful in comparing photocurrent levels from different doping configurations of the device since the photocurrent is also sensitive to series resistances to the contacts. A more relevant comparison figure for different doping levels is the photo-induced voltage: for our device, in the p-n configuration, the photovoltage should be quite large, on the order of the band gap (~ 100 meV). In contrast, in the p-p regions where the photocurrent is the largest, the photothermal voltage estimated from the device resistance ($R \sim 300$ k Ω) and observed current is on the order of $\approx 10 \mu$

eV. Although the photovoltage in the p-n and n-p regions should be significantly larger than in the p-p region, the photocurrent is comparable or smaller due to the very large n-type contact series resistance ($R > G\Omega$).

In previous studies with graphene [22, 30] and metallic nanotubes [26], 2D gate maps such as the one in Fig. 3(a) showed a very characteristic 6-fold rotational symmetry pattern that was used as a fingerprint for identifying a dominating photothermal effect. In contrast, our semiconducting suspended nanotube shows instead a more 4-fold-like pattern. This lack of symmetry finds its origin in the fact that we are working with a semiconducting material with asymmetric n- and p-type contact resistances. In particular, the suppressed PC signal in the n-n region is due to the very large n-type contact resistance ($R > G\Omega$). For graphene (a semi-metal) and metallic SWNTs, the lack of an energy bandgap allows for similarly low p-type and n-type contact resistances, resulting in equal intensity PC signatures both in p-p and n-n regions of the 2D maps, thus forming a 6-fold pattern.

Furthermore, we note that our conclusion for dominant photothermal PC in the p-type regime is in contradiction with a recent work [26] in which it was suggested that the photovoltaic mechanism dominates photocurrent generation in suspended semiconducting nanotubes for all doping configurations. We address these apparent contradictory results by noting that compared to our device, the devices in Ref. [26] had a much lower contact resistance for n-type doping ($\sim 100 \text{ M}\Omega$) and a much higher resistance for p-type doping ($\sim 10 \text{ M}\Omega$). This suggests a more symmetric effective work function alignment in their devices, with the Fermi level of the leads pinned near the mid-gap level (this difference in work function alignment is likely due to the vacuum environment and the vacuum thermal annealing procedure reported, which likely removed an adsorbed water layer on the surface of the silicon oxide in the trench). With the larger Schottky barriers for p-type doping in Ref. [26] the photothermal currents are likely suppressed to a level close to or below the noise floor of the measurement by the large series resistance to the contacts.

Discussion

In summary, we have shown that for the interest of interpreting the origin of photocurrent features in SPCM with semiconducting nanotubes, photothermal effects can absolutely not be a-priori excluded. Similar to systems like graphene and metallic SWNTs, suspended semiconducting SWNTs can show strong photothermoelectric effects through measurement of photothermal currents induced by inhomogeneous illumination.

geneous doping profiles along thermal gradients. However, the dominant or non-dominant character of photothermal currents compared with photovoltaic currents strongly depends on the doping profile of the device and on the n- and p-type contact resistances.

Methods

Sample fabrication. The fabrication of our device began with a p++ silicon wafer used as a backgate covered by 285 nm of thermal silicon oxide. On top of this, gate electrodes made of 5/25 nm W/Pt were defined using electron-beam lithography, followed by the deposition of a 1100 nm thick SiO₂ layer. A 1000 nm deep trench was dry etched, leaving a thin oxide layer on top of the gates. A 5/25 nm W/Pt layer was then deposited to serve as source and drain contacts, and a single-walled carbon nanotube was grown at the last fabrication step at a temperature of 900 °C from patterned Mo/Fe catalysts [31, 28].

SPCM setup. Our SPCM setup [15] consists of a confocal microscope system with the objective ($NA = 0.8$) illuminated by $\lambda = 532$ nm continuous wave collimated laser light. The diffraction limited spot with a measured diameter of ~ 330 nm is scanned across the sample surface by means of two orthogonal galvo-mirrors (x,y) combined to a telecentric lens system while the PC signal as well as the reflected light intensity are recorded simultaneously in order to determine the absolute position of the detected PC features.

Measurements. All measurements presented in this work are performed at atmospheric pressure and room temperature. For SPCM measurement, the source-drain voltage is maintained to 0 V and typical light intensities of 5 kW/cm² are used.

References

- [1] Ahn, Y., Dunning, J. & Park, J. Scanning photocurrent imaging and electronic band studies in silicon nanowire field effect transistors. *Nano Lett.* **5**, 1367–1370 (2005).
- [2] Koren, E., Rosenwaks, Y., Allen, J. E., Hemesath, E. R. & Lauhon, L. J. Nonuniform doping distribution along silicon nanowires measured by kelvin probe force microscopy and scanning photocurrent microscopy. *Appl. Phys. Lett.* **95**, 092105 (2009).

- [3] Allen, J. E., Hemesath, E. R. & Lauhon, L. J. Scanning photocurrent microscopy analysis of silicon nanowire field-effect transistors fabricated by surface etching of the channel. *Nano Lett.* **9**, 1903–1908 (2009).
- [4] Prins, F. *et al.* Fast and efficient photodetection in nanoscale quantum-dot junctions. *Nano Lett.* **12**, 5740–5743 (2012).
- [5] Kasirga, T. S. *et al.* Photoresponse of a highly correlated material determined by scanning photocurrent microscopy. *Nature Nanotech* **7**, 723–727 (2012).
- [6] Balasubramanian, K., Burghard, M., Kern, K., Scolari, M. & Mews, A. Photocurrent imaging of charge transport barriers in carbon nanotube devices. *Nano Lett.* **5**, 507–510 (2005).
- [7] Ahn, Y. H., Tsen, A. W., Kim, B., Park, Y. W. & Park, J. Photocurrent imaging of p-n junctions in ambipolar carbon nanotube transistors. *Nano Lett.* **7**, 3320–3323 (2007).
- [8] Lee, E. J. *et al.* Electronic-band-structure mapping of nanotube transistors by scanning photocurrent microscopy. *Small* **3**, 2038–2042 (2007).
- [9] Freitag, M. *et al.* Imaging of the schottky barriers and charge depletion in carbon nanotube transistors. *Nano Lett.* **7**, 2037–2042 (2007).
- [10] Tsen, A. W., Donev, L. A. K., H.Kurt, Herman, L. H. & Park, J. Imaging the electrical conductance of individual carbon nanotubes with photothermal current microscopy. *Nature Nanotech.* **4**, 108–113 (2008).
- [11] Gabor, N. M., Zhong, Z., Bosnick, K., Park, J. & McEuen, P. L. Extremely efficient multiple electron-hole pair generation in carbon nanotube photodiodes. *Science* **325**, 1367–1371 (2009).
- [12] St-Antoine, B. C., Menard, D. & Martel, R. Position sensitive photothermoelectric effect in suspended single-walled carbon nanotube films. *Nano Lett.* **9**, 3503–3508 (2009).
- [13] St-Antoine, B. C., Menard, D. & Martel, R. Photothermoelectric effects in single-walled carbon nanotube films: Reinterpreting scanning photocurrent experiments. *Nano Res* **5**, 73–81 (2012).
- [14] Nanot, S., Cummings, A. W., Pint, C. L., Ikeuchi, A., Akiho, T., Sueoka, K., Hauge, R. H., Léonard, F., & Kono, J. Broadband, Polarization-Sensitive Photodetector Based on Optically-Thick Films of Macroscopically Long, Dense, and Aligned Carbon Nanotubes. *Sci. Rep.* **3**, 1335 (2013).

- [15] Buchs, G., Barkelid, M., Bagiante, S., Steele, G. A. & Zwiller, V. Imaging the formation of a p-n junction in a suspended carbon nanotube with scanning photocurrent microscopy. *J. Appl. Phys.* **110**, 074308 (2011).
- [16] Allen, J. E., Hemesath, E. R. & Lauhon, L. J. Role of contacts in graphene transistors: A scanning photocurrent study. *Phys. Rev. B* **79**, 245430 (2009).
- [17] Lee, E. J. H., Balasubramanian, K., Weitz, R. T., Burghard, M. & Kern, K. Contact and edge effects in graphene devices. *Nature Nanotech.* **3**, 486–490 (2008).
- [18] Lemme, M. C. *et al.* Gate-activated photoresponse in a graphene pn junction. *Nano Lett.* **11**, 4134–4137 (2011).
- [19] Peters, E. C., Lee, E. J. H., Burghard, M. & Kern, K. Gate dependent photocurrents at a graphene p-n junction. *Appl. Phys. Lett.* **96**, 193102 (2010).
- [20] Xia, F. *et al.* Photocurrent imaging and efficient photon detection in a graphene transistor. *Nano Lett.* **9**, 1039–1044 (2009).
- [21] Park, J., Ahn, Y. H. & Ruiz-Vargas, C. Imaging of photocurrent generation and collection in single-layer graphene. *Nano Lett.* **9**, 1742–1746 (2009).
- [22] Gabor, N. M. *et al.* Hot carrier-assisted intrinsic photoresponse in graphene. *Science* **334**, 648–652 (2011).
- [23] Herring, P. K. *et al.* Photoresponse of an electrically tunable ambipolar graphene infrared thermocouple. *Nano Lett.* **14**, 901–907 (2014).
- [24] Wu, C. *et al.* Elucidating the photoresponse of ultrathin MoS₂ field-effect transistors by scanning photocurrent microscopy. *J. Phys. Chem. Lett.* **4**, 2508–2513 (2013).
- [25] Buscema, M. *et al.* Large and tunable photothermoelectric effect in single-layer MoS₂. *Nano Lett.* **13**, 358–363 (2013).
- [26] Barkelid, M. & Zwiller, V. Photocurrent generation in semiconducting and metallic carbon nanotubes. *Nature Photon.* **8**, 47–51 (2013).

- [27] DeBorde, T., Aspirtarte, L., Sharf, T., Kevek, J. W. & Minot, E. Photothermoelectric effect in suspended semiconducting carbon nanotubes. *ACS Nano* **8**, 216–221 (2014).
- [28] Kong, J., Soh, H. T., Cassell, A. M., Quate, C. F. & Dai, H. Synthesis of individual single-walled carbon nanotubes on patterned silicon wafers. *Nature* **395**, 878–881 (1998).
- [29] Small, J. P., Perez, K. M. & Kim, P. Modulation of thermoelectric power of individual carbon nanotubes. *Phys. Rev. Lett.* **25**, 256801 (2003).
- [30] Song, J. C. W., Rudner, M. S., Marcus, C. M. & Levitov, L. S. Hot carrier transport and photocurrent response in graphene. *Nano Lett.* **11**, 4688–4692 (2011).
- [31] Steele, G. A., Gotz, G. & Kouwenhoven, L. P. Tunable few-electron double quantum dots and Klein tunnelling in ultra-clean carbon nanotubes. *Nature Nanotech.* **3**, 363–367 (2009).

Acknowledgments

The authors acknowledge Val Zwiller for experimental support. This research was supported by a Marie Curie Intra European Fellowship within the 7th European Community Framework Programme (G.B.) and the Netherlands Organization for Scientific Research, NWO (G.A.S.) and the University of Catania (S.B.).

Author contributions

G.B. and S.B. performed the experiments; S.B. fabricated the sample; G.B. and G.A.S wrote the manuscript; all authors discussed the results and contributed to the manuscript.

The authors declare that they have no competing financial interests.

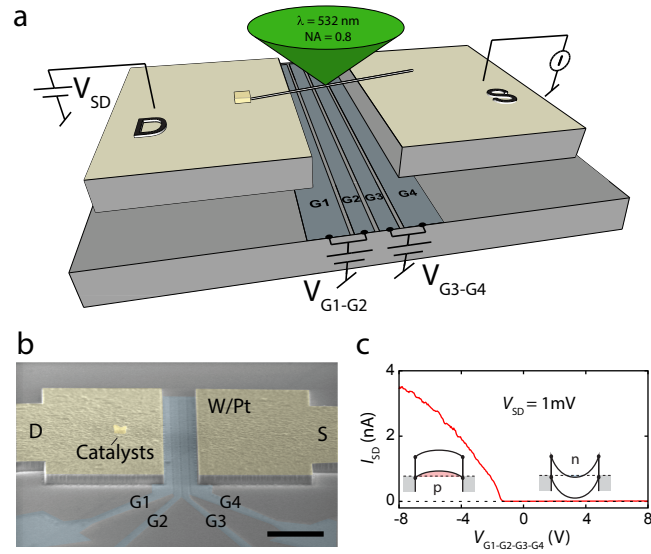


Figure 1: Description and characterization of the device. a) Schematic of the device. Gates G1-G2, G3-G4 are connected to tunable voltage sources V_{G1-G2} and V_{G2-G3} , respectively. The diffraction-limited laser spot ($\lambda = 532$ nm) is accurately positioned along the suspended nanotube axis and induced photocurrent is recorded at the source (S) contact. (b) Scanning electron microscope image of a typical device. Scale bar: $5 \mu\text{m}$. (c) Transistor curve of the device recorded by sweeping gate voltages $V_{G1-G2-G3-G4}$ simultaneously with $V_{SD} = 1$ mV. Onsets: qualitative band diagrams in p- and n-doping regimes, corresponding to "ON" and "OFF" states, respectively.

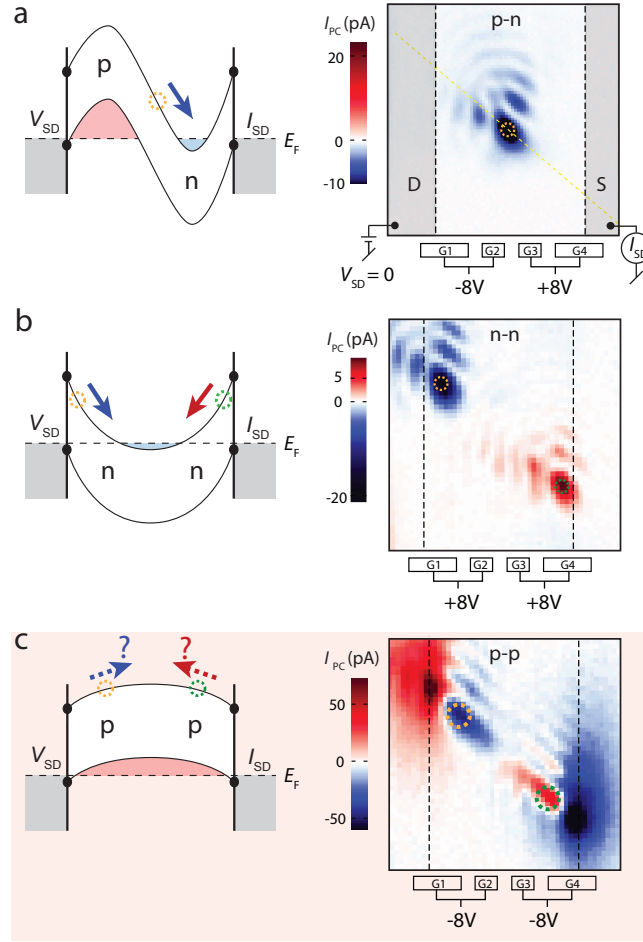


Figure 2: Photocurrent images for different doping configurations. (a)-(c) Qualitative band diagrams (left) and photocurrent images (right) measured for p-n, n-n, and p-p doping configurations, respectively. Location of trench edges (vertical black dashed lines) and gates with applied voltages are indicated. Source (S) and drain (D) contacts with corresponding electrical connections are highlighted in (a) and a yellow dashed line shows the position of the nanotube axis. The location of photocurrent extrema are indicated by dashed circles. The sign of the photocurrent corresponds to the conventional flow notation (red: positive, blue: negative). The arrows on the band diagrams are oriented according to the electron flow notation. Panel (c) illustrates the dominant photothermal mechanism observed in the p-p configuration where electrons are travelling “uphill” (dashed arrows in the band diagram). Patterns around the maximum intensity PC spots in the PC images are due to diffraction effects at the trench gates [15].

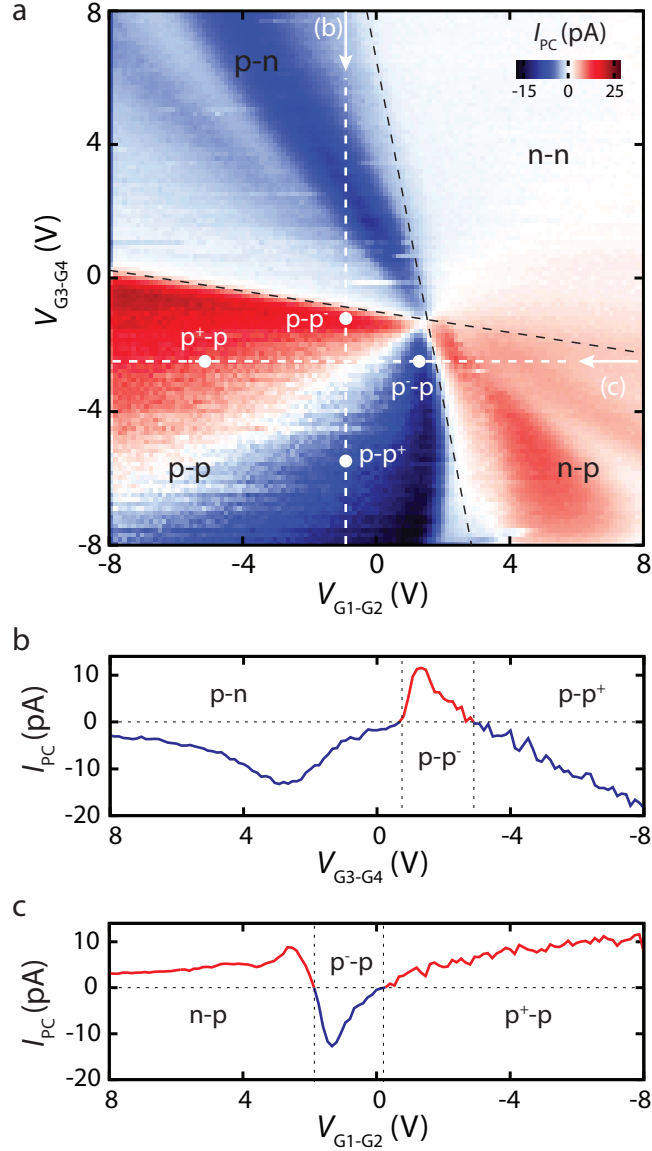


Figure 3: Gate dependence of the photocurrent demonstrating a clear dominating photothermal response. (a) 2D map of the measured photocurrent (I_{PC}) versus V_{G1-G2} and V_{G3-G4} recorded with laser focussed near the middle section of the suspended nanotube, close to the p-n photocurrent minimum shown in Figure 2(a). Black dashed lines delimit four p-n, n-n, n-p and p-p doping regions. (b) and (c) I_{PC} line traces recorded along the horizontal, respectively vertical white dashed lines in panel (a). n-p, p⁻-p and p⁺-p (p-n, p-p⁻ and p-p⁺) doping regions are highlighted.

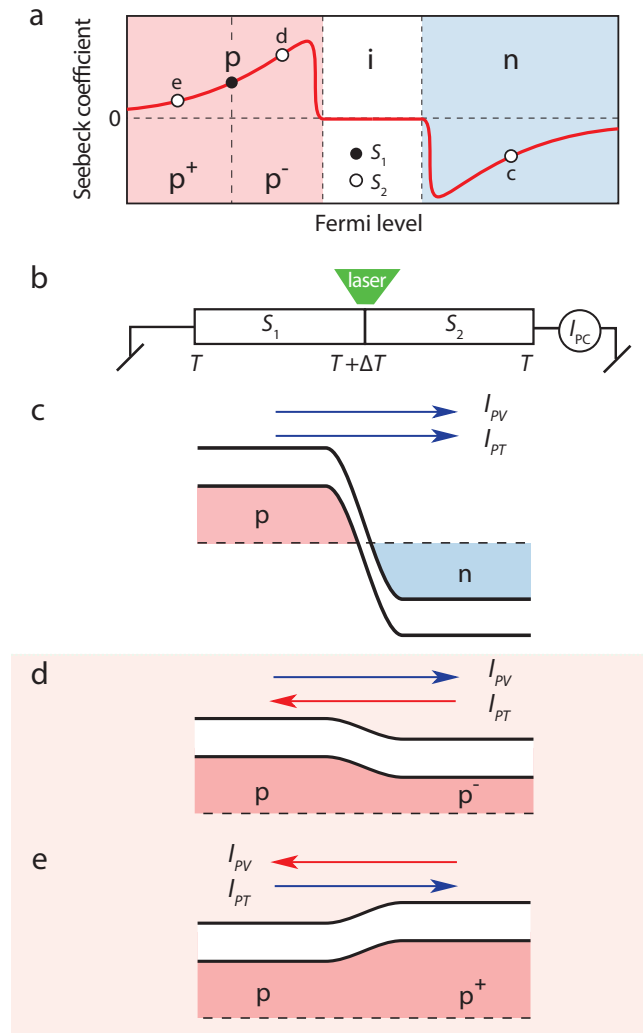


Figure 4: A simple model for photothermal currents travelling against an electric field. (a) Qualitative behavior of the Seebeck coefficient of a semiconducting carbon nanotube versus Fermi level. (b) Thermocouple model with two separately gated nanotube regions with corresponding Seebeck coefficients S_1 and S_2 . Laser excitation region located at the two regions interface gives rise to a temperature increase ΔT . (c) - (e) Band diagrams for p-n, p-p $^-$ and p-p $^+$ doping configurations with corresponding photovoltaic and photothermal current arrows oriented with respect to the electronic flow notation. The color corresponds to the current sign with respect to the conventional flow notation.